

# Revealing and Controlling Energy Barriers and Valleys at Grain Boundaries in Ultrathin Organic Films

Lisa S. Walter, Amelie Axt, James W. Borchert, Theresa Kammerbauer, Felix Winterer, Jakob Lenz, Stefan A. L. Weber, and R. Thomas Weitz\*

In organic electronics, local crystalline order is of critical importance for the charge transport. Grain boundaries between molecularly ordered domains are generally known to hamper or completely suppress charge transfer and detailed knowledge of the local electronic nature is critical for future minimization of such malicious defects. However, grain boundaries are typically hidden within the bulk film and consequently escape observation or investigation. Here, a minimal model system in form of monolayer-thin films with sub-nm roughness of a prototypical n-type organic semiconductor is presented. Since these films consist of large crystalline areas, the detailed energy landscape at single grain boundaries can be studied using Kelvin probe force microscopy. By controlling the charge-carrier density in the films electrostatically, the impact of the grain boundaries on charge transport in organic devices is modeled. First, two distinct types of grain boundaries are identified, namely energetic barriers and valleys, which can coexist within the same thin film. Their absolute height is found to be especially pronounced at charge-carrier densities below  $10^{12} \text{ cm}^{-2}$ —the regime at which organic solar cells and light emitting diodes typically operate. Finally, processing conditions by which the type or energetic height of grain boundaries can be controlled are identified.

## 1. Introduction

Organic semiconductors (OSCs) have enabled a variety of (opto-)electronic devices including organic field-effect transistors (OFETs), organic light emitting diodes (OLEDs), and organic photovoltaics (OPV). Critical performance metrics of these devices are strongly affected by the physical processes that occur at interfaces between layers of different materials, or, different phases within the same material. Examples are the interface between the organic layer and contact metal [1–3]; between the OSC and the gate insulator in an OFET,[4] or between different OSCs at donor–acceptor interfaces in organic solar cells.[5] While such interfaces have been studied in great detail, an interface that is comparably not well understood is the interface between individual (nano-)crystalline domains within an OSC layer of an OLED, OFET or organic solar cell, known as grain boundaries. Inevitable defects

at each of these interfaces can act as sources of trap sites for mobile charge carriers,[6] leading to losses in efficiency of transformation of energy excitations in devices,[7–10] initial and time-dependent degradation,[11–13] hysteresis,[14,15] and reduced charge-carrier mobilities.[4,14,16–18]

Advances in the fundamental understanding of the physical processes at these interfaces and their potential impacts on charge-carrier transport have therefore been essential for enabling improvements to the performance of all optoelectronic devices based on OSCs. However, the detection and simultaneous electrical characterization of grain boundaries has been challenging due to their inherently statistical nature, small scale, and the fact that they are typically hidden within the organic layer.

The most direct impact of grain boundaries on charge transport is typically investigated in FET devices, which is why most impact of grain boundaries on device performance is reported for FETs.

It has been observed that the existence of grain boundaries affects air and bias stability,[11,13] the on–off ratio,[14] the threshold voltage,[14,19] and leads to hysteresis effects.[14] However, the greatest consensus is on the finding that grain boundaries lead to charge-carrier density-dependent,[20,21] and overall reduced mobilities.[16–18,22–24]


L. S. Walter, T. Kammerbauer, F. Winterer, J. Lenz, R. T. Weitz  
Faculty of Physics  
Ludwig-Maximilians-Universität München  
80539 Munich, Germany

L. S. Walter, J. W. Borchert, R. T. Weitz  
I. Institute of Physics  
Georg-August-Universität Göttingen  
37077 Göttingen, Germany  
E-mail: thomas.weitz@uni-goettingen.de

A. Axt, S. A. L. Weber  
Max Planck Institute for Polymer Research  
55128 Mainz, Germany

S. A. L. Weber  
Institute of Physics  
Johannes Gutenberg-Universität Mainz  
55122 Mainz, Germany

R. T. Weitz  
Center for Nanoscience (CeNS)  
Ludwig-Maximilians-Universität München  
80539 Munich, Germany

 The ORCID identification number(s) for the author(s) of this article can be found under <https://doi.org/10.1002/smll.202200605>.

© 2022 The Authors. Small published by Wiley-VCH GmbH. This is an open access article under the terms of the Creative Commons Attribution License, which permits use, distribution and reproduction in any medium, provided the original work is properly cited.

DOI: 10.1002/smll.202200605

Of course, this mobility reduction does not only influence the performance of FETs but also of OLEDs and OPV because here free charge carriers have to diffuse from(to) the electrodes before(after) exciton recombination (dissociation). Moreover, traps in general have been observed to decrease the efficiency of OLEDs by increasing the rate of nonradiative recombination of electron-hole pairs,<sup>[8,10]</sup> and analogously, the efficiency of OPV by increased recombination rates of excitons, i.e., decreased exciton dissociation.<sup>[7,9,12]</sup> While this general impact on recombination rates and device efficiency can likely be attributed to grain boundaries, it is rarely reported<sup>[25–27]</sup> and grain boundaries are mostly avoided in OLEDs and OPV without further explanation.<sup>[28]</sup>

In this work, we present a model system to study the local contribution of grain boundaries in organic semiconducting devices using Kelvin probe force microscopy (KPFM).<sup>[29–31]</sup> KPFM has proven useful to locally characterize grain boundaries both structurally and energetically,<sup>[32–35]</sup> but until now solely applied to films that are several tens of nm thick and/or exhibiting a high density of grain boundaries. Recently, we have demonstrated a drop-casting method for surface-mediated crystallization yielding monolayer-thin films of the prototypical small-molecule OSC *N,N'*-di((*S*)-1-methylpentyl)-1,7(6)-dicyanoperylene-3,4:9,10-bis(dicarboximide) (PDI1MPCN2) with sub-nm roughness even across well-defined grain boundaries and large areas that can be understood as single crystalline thin films.<sup>[36]</sup> While this drop-casting method in its current form is not suitable for large-scale processing, it is sufficient for the current investigations where sample dimensions below 1 cm<sup>2</sup> are required. The high purity of the resulting films is comparable to recent works focusing on low-dimensional organic crystals as the active layer in, e.g., OFETs,<sup>[37–40]</sup> and allows precise examination of the surface potential of individual grain boundaries. In particular, this allows detailed local electrostatic examination of grain boundaries and thereby enables identification of the mechanisms by which grain boundaries can affect charge transport. In addition, using electrostatic gating, the charge-carrier density in the monolayer-thin films can be tuned in situ up to  $\approx 10^{12}$  cm<sup>-2</sup>, allowing measurements of the energetics at grain boundaries at charge-carrier densities relevant in organic solar cells (operated typically at charge-carrier densities of  $10^9$ – $10^{10}$  cm<sup>-2</sup>),<sup>[41,42]</sup> OLEDs ( $10^{10}$ – $10^{11}$  cm<sup>-2</sup>),<sup>[7]</sup> and OFETs ( $10^9$ – $10^{12}$  cm<sup>-2</sup>).<sup>[4]</sup>

## 2. Surface Potential Within A Single Crystal Grain

A schematic of the measurement setup and the devices under investigation is shown in **Figure 1a**. The samples consist of a PDI1MPCN2-covered Si/Al<sub>2</sub>O<sub>3</sub> wafer (see the Experimental Section for fabrication details). The organic films are characterized by large, highly crystalline grains, separated by well-defined grain boundaries (e.g., cf. **Figure 2**).<sup>[36]</sup> According to X-ray diffraction measurements, films of 1.8 nm thickness correspond to monolayers.<sup>[36]</sup> In the shown setup, the charge-carrier density  $n$  in the PDI1MPCN2 thin films can be tuned precisely by the gate voltage  $V_{GS}$ . Its impact on the surface potential  $U_{SP}$  is detected after reaching electrostatic equilibrium, that is, no additional electric field is applied parallel to the molecular layer

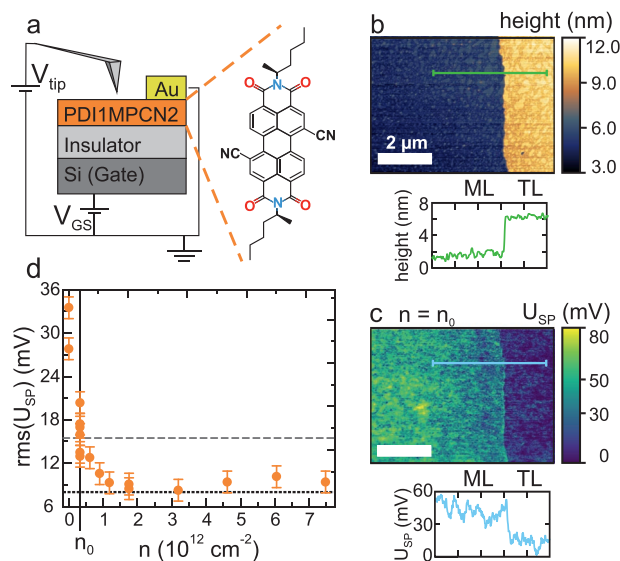


**Figure 1.** Detection of the surface potential under varying charge-carrier density. a) Scheme of the device geometry and the measurement setup. b,c) Topography and surface potential at zero external charge-carrier density  $n_0$ , respectively, with profiles across the indicated lines and indicated position of monolayer (ML) and trilayer (TL). d) Charge-carrier density-dependent  $\text{rms}(U_{SP})$ . Data were extracted from the scans shown in Figure S2 in the Supporting Information. The gray dashed line is the mean value of  $\text{rms}(U_{SP})$  at  $n_0$  taken from (c) and serves as a reference. The black dotted line is the resolution limit taken from Figure S1 in the Supporting Information. Data points are the rms value extracted from a slab of 0.5  $\mu\text{m}$  in the  $y$ -direction; the errors are estimated to 1.5 mV due to extraction uncertainties in the choice of the slab width. All scale bars are 2  $\mu\text{m}$ .

and we have not performed time-dependent measurements on electric charging or current flow. The surface potential  $U_{SP}$  is the sum of the potential induced by  $V_{GS}$  and the contact-potential difference (CPD)  $U_{CPD}$  measured at  $V_{GS} = 0$  (see the Supporting Information for details). If  $V_{GS} = 0$ , no external charge carriers are induced in the OSC and we refer to zero external charge-carrier density  $n = n_0$ . In the following, measurements at  $n_0$ , where  $U_{SP} = U_{CPD}$ , serve as reference for measurements with increased charge-carrier density.

As baseline for our measurements, we first discuss the surface potential within a crystalline grain of the PDI1MPCN2 monolayer-thin film. A typical topography and surface-potential map of such a region including a monolayer-trilayer step is shown in **Figure 1b,c**. The topographical smoothness of the clean solution-deposited thin-films can be discerned by the small values for the rms roughness of 0.6 nm. To quantify the variation of the surface potential within a single grain, the  $\text{rms}(U_{SP})$  was extracted, e.g. to 15 mV for the scan at  $n_0$  (dashed line in **Figure 1d**). Since the detected potential landscape does not change during subsequent scans and is well above the noise level of 8 mV (**Figure S1**, Supporting Information), it can be attributed to defects or charge inhomogeneities at the semiconductor-dielectric interface. This is consistent with the observation that OSC films on Al<sub>2</sub>O<sub>3</sub> show smaller  $\text{rms}(U_{SP})$  than films on SiO<sub>2</sub> (see **Table S1**, Supporting Information), highlighting the role of the substrate.

The surface-potential variations can be understood as energetic disorder which may hinder charge-transport even within

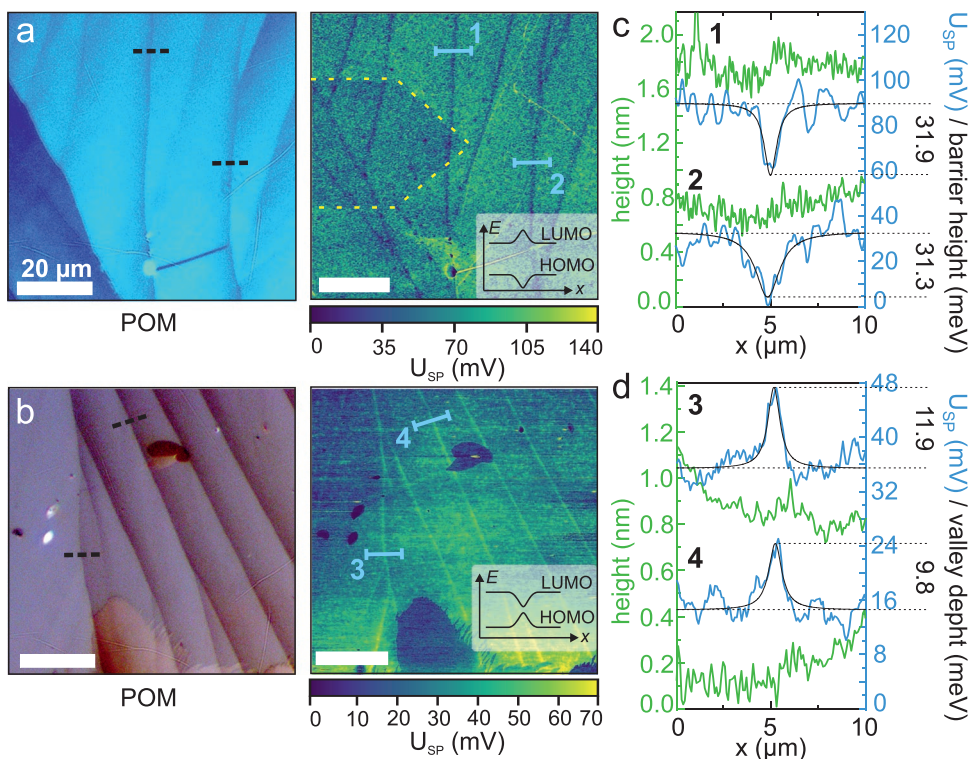


**Figure 2.** Kelvin probe force microscopy at grain boundaries. a,b) POM image (left) and surface potential (right) at two positions of a monolayer film displaying (a) barriers and (b) valleys at  $n_0$ . The insets show the schematic of HOMO and LUMO for the barrier and valley, respectively. The visible shadow of the cantilever highlighted by the yellow dashed line is discussed later in the main text. c,d) Extracted profiles of topography (cf. Figure S5, Supporting Information) and surface potential along the shown lines in (a) and (b), respectively, with Lorentzian fits and calculated barrier heights (fit error 0.7 meV) and valley depths (fit error 2.7 meV), respectively. The graphs are artificially offset for clarity. All scale bars are 20  $\mu\text{m}$ .

single grains and thereby lead to a reduction of charge-carrier mobility. To study the impact of the observed surface-potential variations on charge transport, we increased the charge-carrier density by electrostatic gating and detected the change in  $\text{rms}(U_{SP})$ , shown in Figure 1d. If  $n$  is increased above  $n_0$  (by application of a positive  $V_{GS}$ ), the  $\text{rms}(U_{SP})$  is found to decrease until saturating above  $n \approx 2 \times 10^{12} \text{ cm}^{-2}$  to the resolution limit, while it increases significantly if  $n$  is reduced to zero due to the absence of screening caused by the depletion of charge carriers within the film. Since we are able to tune the charge-carrier density between  $n = 0$  and above  $10^{12} \text{ cm}^{-2}$ , our investigations are performed under conditions in which OLEDs, OFETs and organic solar cells typically operate. Especially in the density region below  $10^{12} \text{ cm}^{-2}$  (typical for OLEDs and organic solar cells), notable surface-potential variations are present, even though our films are highly crystalline. It can be expected that the potential landscape of OSCs in OLEDs and organic solar cells shows even higher energetic disorder and therefore a stronger impact on charge-carrier mobility, as these films are typically disordered.

In passing we note, that at the step edge, no spike in the surface potential is present as has been found by KPFM in bulk single crystals.<sup>[43]</sup> Instead, the trilayer shows an overall smaller surface potential than the monolayer (cf. Figure S4, Supporting Information). This can be attributed to screening of the built-in gate potential by the sheet of mobile charges that forms in the molecular layer close to the insulator.<sup>[44]</sup> This is further

confirmed by the observation that in the absence of screening, i.e., at  $n = 0$ , the potential step at the monolayer-trilayer transition disappears (cf. Figures S2, S4, Supporting Information).

### 3. Surface Potential at Grain Boundaries

In Figure 2, we show a polarized optical microscopy (POM) image and a KPFM scan at  $n_0$  of two exemplary monolayer-thin regions of the PD11MPCN2 film including grain boundaries. The corresponding topography scans are displayed in Figure S5a,b in the Supporting Information. From the given line profiles in Figure 2c,d across four representative grain boundaries, it becomes clear that the grain boundaries observable in POM are not accompanied by a change in film height. This is in direct contrast to OSC films evaporated onto insulating substrates, which predominantly display some degree of 3D island growth with a high density of step edges during the sub-monolayer growth stage before connected monolayers can grow to cover a significant area.<sup>[32,34,35]</sup> Here, only the KPFM scans in Figure 2 clearly reveal the grain boundaries by a contrast in the CPD and a dip or a peak in the line profile. The CPD contrast can be translated into a local work-function variation and therefore to the bending of the semiconductor's highest occupied molecular orbital (HOMO) and lowest unoccupied molecular orbital (LUMO). Moreover, a clear differentiation can be made between grain boundaries showing a smaller

CPD than surrounding grains (called barriers in the remainder, Figure 2a,c) and those with higher CPD (called valleys, Figure 2b,d). Finally, we would like to point out that in thicker films on the same substrate (bottom of Figure 2b) even though grain boundaries are visible in the POM images, they are not visible in KPFM (compare also Figure S5c, Supporting Information). Hence, grain boundaries in films that are several tens of nm thick and therefore suitable for OLEDs and OPV cells, will likely not be identifiable with this technique. This finding underlines that monolayer films are an ideal model system to investigate energetics at grain boundaries.

Grain boundaries of different type (i.e., barriers and valleys) have been theoretically predicted, e.g., for pentacene thin films,<sup>[45]</sup> and monolayers of PDI1MPCN2,<sup>[46]</sup> but have not been observed in experiment. Specifically, the HOMO and LUMO at grain boundaries bend in an inverted manner,<sup>[46]</sup> i.e., barriers are characterized by upward(downward) bending of the LUMO (HOMO), resulting in an increased band gap (cf. inset of Figure 2a), and vice versa for valleys (inset of Figure 2b). This is the reason for the above assignment of barriers(valleys) to grain boundaries with a smaller(higher) CPD than surrounding grains (see the Supporting Information for a full derivation). In experiments however, it has not been clear if measured differences in CPD at grain boundaries are due to processing conditions,<sup>[6,23,47]</sup> the sign of trapped charges,<sup>[17,19]</sup> the n- or p-type character of the semiconductor,<sup>[32]</sup> or variations in the film thickness.<sup>[34]</sup> Our measurements reveal that none of these conditions can be the only determining factor for the existence of barriers or valleys, since all our films are deposited under similar conditions and are smooth across the grain boundaries. **Figure 3** even displays both types in the same film. To our knowledge, this is the first time that the theoretically predicted coexistence of two distinguishable types of grain boundaries was experimentally proven.

To quantify the differences between valleys and barriers, we determined valley depths and barrier heights by extracting the difference of the CPD between grain boundaries and neigh-

boring grains<sup>[48]</sup> (for evaluation details see Section C in the Supporting Information). While valleys act as traps thereby leading to a reduction of the mobility,<sup>[6,49]</sup> just recently it was shown that barriers impede charge transport more significantly than valleys due to a back-reflection of charges.<sup>[46]</sup> Because of these different mechanisms of trapping and backscattering, previous reports on “barrier heights” or “trap depths” determined by c-AFM,<sup>[19]</sup> or activated charge-transport,<sup>[50]</sup> can only refer to trap-like grain boundaries, that is, valley depths. As indicated in Figure 2 and **Figure 4**, we find valley depths around 10–20 meV and barrier heights from 30 to 60 meV. Note that the valley depths and barrier heights given here, in contrast to transport measurements, do not include transport-limiting factors such as contact resistance or trapping at the semiconductor-insulator interface. Additionally, it is per se unclear how the process of backscattering of charge carriers at barrier-like grain boundaries will show up in activation measurements.

#### 4. Impact of Charge-carrier Density on Barrier Height and Valley Depth

OLEDs and organic solar cells operate at different charge-carrier densities ( $10^9$ – $10^{11}$  cm<sup>-2</sup>),<sup>[7,41,42]</sup> than OFETs ( $10^{12}$  cm<sup>-2</sup>).<sup>[4]</sup> Since absolute values of the observed barrier heights and valley depths have been predicted to decrease with increasing charge-carrier density,<sup>[21]</sup> a careful analysis of the barrier height/valley depth at different charge-carrier densities is required. This investigation will help to assess the respective relevance of grain boundaries for charge transport in the different device types. To this end, we have used two strategies of charge-carrier density control, namely electrostatic gating and photoexcitation. Please note that the influence of only one type of charge carrier is investigated within one experiment (electrons in electrostatic gating and holes via optical excitation, cf. Section D, Supporting Information), so that the results are relevant to transport processes in OFETs and in OLEDs(OPV) before(after) exciton formation(separation). Even more, both injection strategies are assumed to be reversible processes, that is, the surface potential reaches its original distribution after discharging the thin film.

Figure 4 displays KPFM scans of areas with a barrier (Figure 4a) and three valleys (Figure 4c), where the charge-carrier density was increased electrostatically, analogously to the measurements for the single grain shown above. The barrier heights and valley depths clearly decrease with increasing charge-carrier density, and completely disappear in the noise floor at the highest investigated charge-carrier densities. We anticipate that the processes leading to the disappearance of valleys and barriers differ for the two types: In valleys, the electrons are trapped due to the band bending where they act as repulsive sites for subsequently injected electrons,<sup>[45]</sup> thereby making the valley itself energetically less favorable. This is equivalent to the flattening of the LUMO and a decrease of the CPD contrast between grain and grain boundary, i.e., a reduction of the valley depth up to its complete disappearance as seen in Figure 4b,d (for line profiles see Figures S6 and S7, Supporting Information). Conversely, electrons are backscattered from barriers and remain within the energetically more favorable grains,<sup>[21,51]</sup> and raise the LUMO levels of the grains

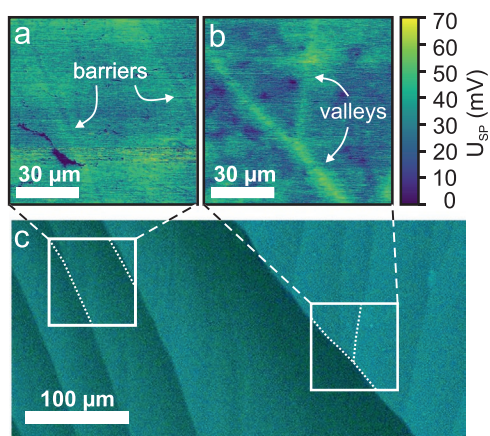


**Figure 3.** Coexistence of barriers and valleys. a) Surface potential of two barriers. b) Surface potential of two valleys. c) POM image of a thin film of PDI1MPCN2, where the areas of (a) and (b) and the courses of the respective grain boundaries are marked. A large-scale scan was performed to exclude degradational effects, shown in Figure S11 in the Supporting Information.

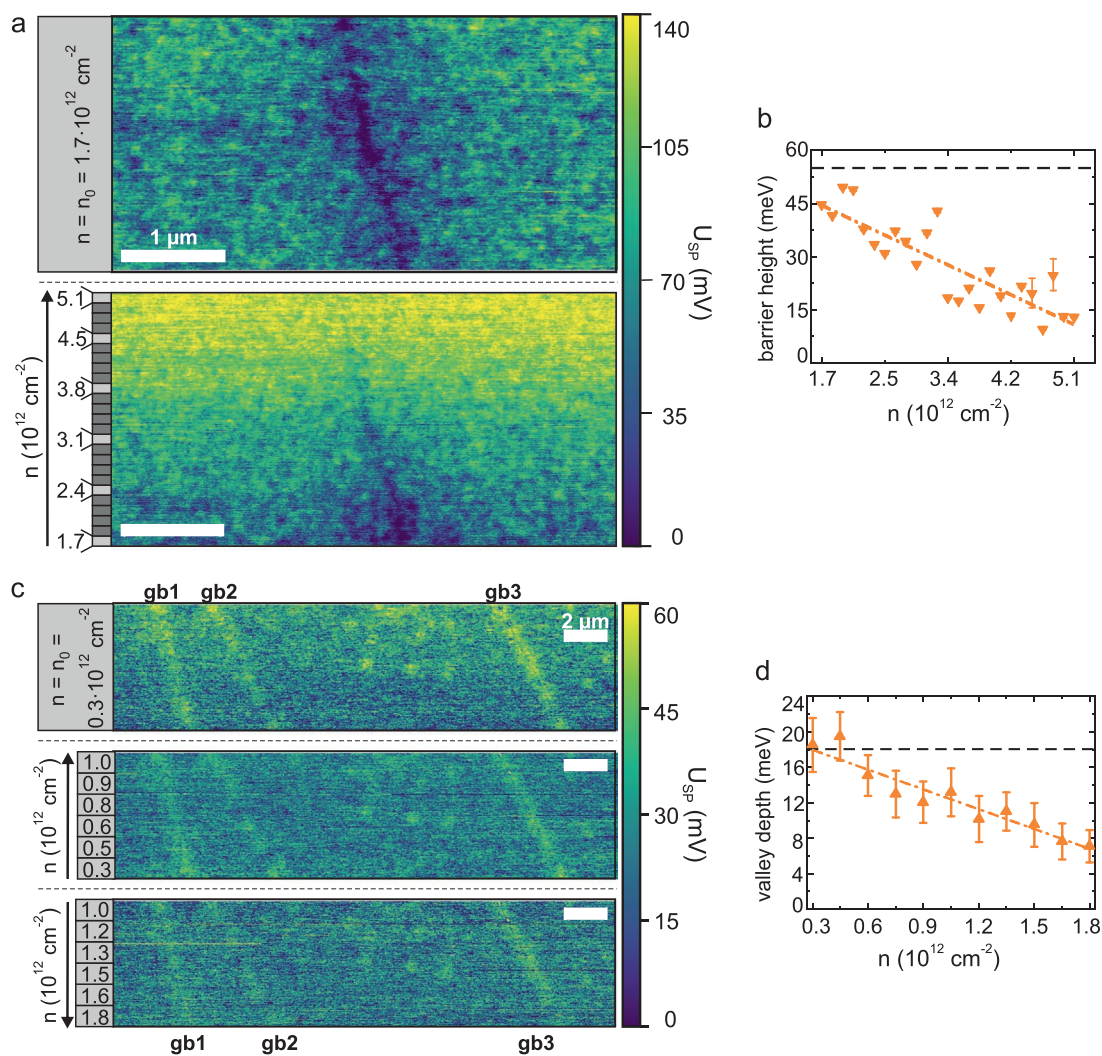


**Figure 4.** Charge-carrier density dependent barrier height and valley depth. a) KPFM scan of a barrier at  $n_0$  (top) and varying electron density as indicated (bottom). The arrow corresponds to the scan direction; scale bars are  $1 \mu\text{m}$ . b) Barrier height extracted from (a) as function of electrostatically induced charge-carrier density. The dashed line is the mean barrier height at  $n_0$ . The dashed-dotted line serves as guide to the eye. c) Surface potential of three valleys at  $n_0$  (top) and varying charge-carrier density as indicated (middle, bottom). Arrows indicate the scan direction; scale bars are  $2 \mu\text{m}$ . A plane level fit was done for the figures with varying  $n$ , but further evaluation was conducted with nonflattened images. d) Valley depth of gb3 as function of electrostatically induced charge carrier density. The dashed line is the mean valley depth at  $n_0$ . The dashed-dotted line serves as guide to the eye. Each data point was extracted from Lorentzian fits at line profiles leveled over a) 15 or c) 35 lines; errors are calculated from fit errors using error propagation. For evaluation details see the Supporting Information.

until the bands are flat,<sup>[52]</sup> and the energetic landscape for all following electrons is the same for grains and valleys.

Notably, the barriers and valleys are only screened if the electrostatically induced charge-carrier density increases to values above  $10^{12} \text{ cm}^{-2}$ . While OFETs are typically operated at such high charge-carrier densities, OLEDs and organic solar cells typically operate at  $n < 10^{11} \text{ cm}^{-2}$  and therefore barriers and valleys, as well as charge inhomogeneities within the film, will significantly impact charge transport in these devices.

So far, we have successfully demonstrated the impact of electrons on the energetic landscape by injecting them electrostatically. Since in OLEDs and organic solar cells it is also possible that small densities of holes accumulate in the electron-conducting film, which then act as recombination sites for subsequently injected electrons, we further studied the impact of a

small density of holes on the potential distribution. However, the electrostatic injection of holes into PDI1MPCN2 is hindered by the high hole-injection barrier of gold, the small HOMO-overlap in PDI1MPCN2, as well as deep hole traps at  $6.0 \text{ eV}$  (the  $E_{\text{HOMO}}$  of PDI1MPCN2 is  $6.74 \text{ eV}$ <sup>[53]</sup>) localized in clusters of residual water,<sup>[54]</sup> small amounts of which can be present in our inert atmosphere.<sup>[55]</sup> Therefore, we illuminated our samples with a standard halogen lamp ( $150 \text{ W}$ ) to form excitons in the OSC thin film (cf. Table S2, Supporting Information), part of which are separated into electrons and holes by the built-in potential at the insulator–semiconductor interface or within the semiconductor. Since our data are consistent with no additional electrons in the film, as we will discuss below, we anticipate that the optically induced electrons are drained by water ions.<sup>[56]</sup> To directly compare the pristine to the slightly hole-doped film,

we have shadowed part of the film with the approached cantilever during illumination and mapped the potential landscape in the dark subsequently (Figure 2a and Figure S8, Supporting Information). Notably, the surface potential increases by 20 mV in the illuminated part, while neither the  $\text{rms}(U_{\text{SP}})$  nor the barrier height seem to be affected by the small density of induced charge carriers (cf. Figure S9, Supporting Information). The increased  $U_{\text{SP}}$ , the sharpness, as well as the observed stability of the potential difference over several hours in the dark, are consistent with an increased density of immobile positive charge carriers generated by light (that are most likely trapped in deep traps in the film). We assume that these hole traps are the same that have previously been identified by transport measurements,<sup>[54]</sup> now first observed in real space by our measurements. Since those traps are presumably located not in the OSC molecules and deeper in energy compared to the potential irregularities within single grains or at grain boundaries, the density of trapped holes increases homogeneously in the entire organic thin film and the barrier heights remain constant. Our measurements thus reveal that while trapped minority carriers will act as recombination sites for majority carriers, they do not change the energetics at the grain boundaries.

## 5. Toward Controlling Energetics at the Grain Boundary Through Processing

A final point pertains the question how the grain boundaries acting as valleys or barriers emerge physically. Identifying the structural cause and/or the parameters in film formation leading to valleys or barriers would be helpful to improve future OSC devices. It is known, that the direct surrounding of each molecule changes its polarization energy,<sup>[6]</sup> and consequently, structural changes such as differences in local packing and/or a change in the distance of the molecules across a grain boundary can lead to locally varying HOMO-LUMO gaps. While the resolution of our measurements is not high enough to resolve the local molecular orientation within a grain, we have found examples in which noticeable dips in the topography of about 0.5 nm were visible (Figure S10, Supporting Information) going along with barriers in the energetic landscape (none were found for valleys). This indicates that larger intermolecular distances can lead to barriers, which is consistent with results obtained by simulations of the polarization field and charge-quadrupole interaction energies across grain boundaries in pentacene films.<sup>[45]</sup> However, we also found barriers in other parts of the film without such dips in the topography, indicating that also changes in molecular orientation, lowering the orbital overlap between neighboring molecules, can lead to both types of grain boundaries as proposed by theoretical calculations.<sup>[45,46]</sup>

In order to find a link between the film formation and the emergence of valleys and barriers, we have investigated the surface potential at 30 positions on 12 individual thin films, and related it to the processing conditions (Section E, Supporting Information). Doing so, we found a relation between the nature of the grain boundaries within a thin film and its shape, emerging from the thin-film fabrication. During the deposition process, a solution of PDI1MPCN2 is drop-cast onto the substrate where the outline of the droplet can pin at its ini-

tial position due to the surface energy contrast on a patterned substrate.<sup>[36]</sup> While circular spots with a homogeneous outline are obtained from such pinned droplets, a smeared noncircular film with wavy or uneven borders can emerge if the droplet does not pin but moves or shrinks while drying. Using these definitions, we found solely valleys in perfectly pinned films and only barriers in depinned (smeared) films. Even more, both types of grain boundaries could be observed within the same organic thin film (Figure 3) in a region between a pinned and a smeared part (cf. Figure S11, Supporting Information). This implies that the complex and not yet fully understood dynamics of thin film crystallization during the PDI1MPCN2 deposition determines the type of the grain boundary. Summarizing, we can a priori control if a thin film will contain only one type of grain boundary by choosing the processing conditions such that the drop-cast solution will pin or smear while drying.

In this context, the substrate only plays a minor role: as mentioned before, we observed that the roughness of the film only impacts the energetic disorder and therefore the  $\text{rms}(U_{\text{SP}})$  of the crystalline areas of the films (also compare Table S1, Supporting Information). However, we could observe both pinned and smeared films, and therefore also the emergence of barriers and valleys, on two different insulators, that is, silicon oxide and aluminum oxide (cf. Table S3, Supporting Information).

Finally, we observed that the solvent choice impacts the energetics at grain boundaries. Overall, less pronounced valleys and barriers at grain boundaries were measured in films produced from toluene-containing solutions (see Figures S12 and S13 and Table S3, Supporting Information).

In passing we note that an idealized thin-film fabrication can be formulated by the aim to achieve films without barriers (as they hinder charge transport more effectively than valleys<sup>[46]</sup>), as few valleys as possible with the smallest possible depth, and as smooth as possible crystal grains. According to our observations, these films are obtained by perfectly pinned droplets containing toluene on smooth substrates. This summary matches with the preparation methods originally suggested for this molecule, as such films have consistently shown increased mobilities.<sup>[36]</sup>

## 6. Conclusion

By using high-sensitivity heterodyne KPFM imaging of grain boundaries within a monolayer thin, highly crystalline organic semiconducting PDI1MPCN2 film, we were able to identify energetic barriers and valleys at grain boundaries, define thin-film processing conditions under which they emerge, and investigate their behavior under electrostatically controlled charge-carrier density. The use of monolayer-thin films was essential to characterize the highly pure, well-defined single grain boundaries in a minimal model system under inert and reversible conditions. By tuning the charge-carrier density electrostatically, we could simulate the impact on charge transport during the operation of organic semiconductor devices. From the different energetic distributions of the two grain-boundary types, we were able to separate the different mechanisms of trapping at valleys and backscattering at barriers at charge-carrier densities less than  $10^{12} \text{ cm}^{-2}$ . This importantly corresponds

to the density range where OLEDs and OPV cells typically operate, thus highlighting the role of grain boundaries as well as potential irregularities in the thin films that lead to a suppression of charge transport in these systems. Likewise, OFETs will be significantly impacted in the transition between the “on” and “off” states of the transistor where low charge-carrier densities are also present.

We have focused our work on a prototypical perylene-diiimide semiconductor, an organic dye which is often used in optoelectronic devices, but the general concept of valleys and barriers and their presence in thin films may also hold for other materials used as transport layers in OLEDs, OPV, and OFETs. In addition, the insights from this work may prove useful for researchers investigating charge transport in other optoelectronic materials systems such as perovskites,<sup>[57]</sup> metal oxides,<sup>[58]</sup> and transition metal dichalcogenides,<sup>[59,60]</sup> where grain boundaries might occur and lead to loss in transport or energy transformation processes.

## 7. Experimental Section

**Sample Preparation:** The n-type OSC used in this work is the core cyanated perylene diimide *N,N'*-di((S)-1-methylpentyl)-1,7(6)-dicyanoperylene-3,4:9,10-bis(dicarboximide) (PD11MPCN2) shown in Figure 1a, whose crystallization behavior, mechanical, and electrical properties have been investigated before.<sup>[4,36,46,61,62]</sup> The preparation of monolayer-thin films by drop-casting was presented and established in previous work<sup>[36]</sup> and accordingly used here as follows: 15 × 20 mm<sup>2</sup>-sized substrates of highly doped silicon with 30 nm Al<sub>2</sub>O<sub>3</sub> or 300 nm SiO<sub>2</sub> were cleaned in acetone and isopropanol for 10 min each and by a subsequent etching step in an oxygen plasma at 50 W for 7 min (Diener Pico Plasma cleaner). The substrates were coated with a tetradecylphosphonic acid (TDPA, used for Al<sub>2</sub>O<sub>3</sub> substrates) or octadecyltrichlorosilane (ODTS, used for SiO<sub>2</sub> substrates) SAM, respectively, from which circles of 5 or 6 mm diameter were etched away using the same conditions as before. A solution of 0.1 wt% PD11MPCN2 (BASF) in DMP or DMP:Toluene mixtures was dissolved, stirred, filtered, and drop-cast onto the etched circles. The samples were dried on a hotplate at 70 °C over night. Also see Figure S13 and Table S3 in the Supporting Information for details on how to achieve pinned or smeared films. As proposed by previous XRD measurements (cf. the Supporting Information of ref. [36]), to assure mono- (1.8 nm thickness) to bilayer (3.6 nm) thin films, the step height was measured down to the substrate for some samples using AFM (Bruker Dimension 3100) in tapping mode. 40 nm Au were thermally evaporated before(after) dropcasting in order to build bottom gate bottom(top) contact devices.

**Optical Characterization:** Grain boundaries were located using POM (Zeiss Axio Scope.A1) and a complete spot of the organic thin film was mapped. Large crystallites at the border and in the middle of the drops as well as thicker layers served as guides during KPFM measurements and for assembling the taken pictures to the overview images.

**KPFM Measurements:** All KPFM measurements were performed as sketched in Figure 1a in an Argon glove box at 26 °C to avoid bias stress and degradational effects (while perylene diimides are generally known to show minimal air degradation,<sup>[63]</sup> stability under bias stress has been observed to increase with the number of grain boundaries and can be assumed to be small at measurements in solution processed thin films<sup>[11,13]</sup>). An Asylum research MFP3D SFM and a PtIr coated tip (SCM-PIT-V2, with spring constant  $k = 3.0 \text{ N m}^{-1}$ , tip radius  $r = 25 \text{ nm}$ ) were used. The KPFM signal was detected in FM heterodyne mode using a Zurich Instruments HF2 Lock-in amplifier with AC and DC voltage applied to the tip (tip bias). For the exact circuit diagram cf. ref. [31]. The gate voltage was applied via Output 3 of the HF2 Lock-in

amplifier. Source and drain as well as all outer conductors and the glove box casing were set to the same ground. For measurements at  $n_0$ , the gate was set to ground as well. For the light-dependent measurements, samples were used without evaporated contacts, but grounded by silver paste at the border of the sample. The samples with the built-in halogen lamp (150 W) of the AFM camera were illuminated with the tip approached to the surface, then it was turned off and scanning was started. To reduce effects of the ambient light, the glovebox was covered with a curtain. Impact of the detection laser was excluded with a wavelength of 860 nm, as it was turned on all the time, such that the cantilever shadow would not be observed in Figure 2. An overview over differences in the conducted experiments is shown in Figure S8 in the Supporting Information.

**Statistics:** Within the scope of this work, the surface potential was investigated at 30 positions on 12 individual thin films (Table S3, Supporting Information). All presented AFM data were preprocessed using the software Gwyddion,<sup>[64]</sup> by the following procedure: 1) Rows of KPFM scans were aligned by the mean of differences. If necessary, the plane was leveled additionally by mean plane subtraction for a better view of the scans, but data were extracted from nonleveled scans. The lowest point was set to zero. Line-profiles were extracted with a width slightly smaller than the number of lines with constant gate voltage to account for the time-dependent charging effect of the semiconductor.  $rms(U_{SP})$  values were extracted using the statistics tool of Gwyddion for areas with a corresponding slab width, by varying this width slightly, the error was estimated to 1.5 mV for all extracted  $rms(U_{SP})$  values. 2) Topography scans were leveled by mean plane subtraction. For large scans (>50 × 50 μm<sup>2</sup>) a polynomial background of 2nd order was subtracted additionally. The rows were aligned by a polynomial of 2nd order while extracting high features by a mask tool. The lowest point was set to zero. Line profiles were extracted at the exact same conditions as for the corresponding KPFM scan and compared to them by position. 3) Extracted line profiles across grain boundaries were fitted by a Lorentzian using the software Origin, the mathematical details are described in Section C in the Supporting Information. The given barrier heights or valley depths refer to the fit values, errors are fit errors using error propagation. 4) Charge-carrier densities have been calculated from the applied gate voltage using a plate capacitor model for the field-effect transistor, detailed in Section B in the Supporting Information.

## Supporting Information

Supporting Information is available from the Wiley Online Library or from the author.

## Acknowledgements

L.S.W. and R.T.W. acknowledge funding from the Center for Nanoscience (CeNS) and the SolarTechnologies go Hybrid (SolTech) initiative. The authors additionally acknowledge funding by the Deutsche Forschungsgemeinschaft (DFG, German Research Foundation) under Germany's Excellence Strategy and “EXC 2089/1–390776260 (e-conversion).” The authors additionally acknowledge insightful discussions with PD Dr. B. Nickel and Prof. P. W. M. Blom.

Open access funding enabled and organized by Projekt DEAL.

## Conflict of Interest

While during the cause of the study A.A. was employed at the Max Planck Institute for Polymer Research, currently she is employee at Oxford, the manufacturer of Asylum AFMs such as the one used for this study.

## Author Contributions

The experiments were conceived and designed by L.S.W. and R.T.W. L.S.W. prepared the samples, conducted the measurements and data analysis. A.A. and S.A.L.W. helped with the measurements, T.K. helped with the sample preparation. All authors discussed the data. L.S.W. and R.T.W. wrote the manuscript with the input of all authors.

## Data Availability Statement

The data that support the findings of this study are available from the corresponding author upon reasonable request.

## Keywords

2D-crystals, energy transformation, grain boundary, Kelvin probe force microscopy, organic semiconductors

Received: February 25, 2022

Revised: July 11, 2022

Published online: July 29, 2022

- [1] M. Waldrip, O. D. Jurchescu, D. J. Gundlach, E. G. Bittle, *Adv. Funct. Mater.* **2019**, *39*, 1904576.
- [2] S. Braun, W. R. Salaneck, M. Fahlman, *Adv. Mater.* **2009**, *21*, 1450.
- [3] N. B. Kotadiya, H. Lu, A. Mondal, Y. Ie, D. Andrienko, P. W. M. Blom, G.-J. A. H. Wetzelaer, *Nat. Mater.* **2018**, *17*, 329.
- [4] I. Vladimirov, S. Müller, R.-P. Baumann, T. Geßner, Z. Molla, S. Grigorian, A. Köhler, H. Bässler, U. Pietsch, R. T. Weitz, *Adv. Funct. Mater.* **2019**, *29*, 1807867.
- [5] R. Steim, F. R. Kogler, C. J. Brabec, *J. Mater. Chem.* **2010**, *20*, 2499.
- [6] H. F. Haneef, A. M. Zeidell, O. D. Jurchescu, *J. Mater. Chem. C* **2020**, *8*, 759.
- [7] M.-J. Tsai, H.-F. Meng, *J. Appl. Phys.* **2005**, *97*, 114502.
- [8] R. A. Street, M. Schoendorf, A. Roy, J. H. Lee, *Phys. Rev. B* **2010**, *81*, 205307.
- [9] M. Kuik, G.-J. A. H. Wetzelaer, H. T. Nicolai, N. I. Craciun, D. M. de Leeuw, P. W. M. Blom, *Adv. Mater.* **2014**, *26*, 512.
- [10] S. R. Cowan, A. Roy, A. J. Heeger, *Phys. Rev. B* **2010**, *82*, 245207.
- [11] S. Müller, R.-P. Baumann, T. Geßner, R. T. Weitz, *Phys. Status Solidi RRL* **2016**, *10*, 339.
- [12] S. Scholz, D. Kondakov, B. Lüsse, K. Leo, *Chem. Rev.* **2015**, *115*, 8449.
- [13] R. T. Weitz, K. Amsharov, U. Zschieschang, M. Burghard, M. Jansen, M. Kelsch, B. Rhamati, P. A. van Aken, K. Kern, H. Klauk, *Chem. Mater.* **2009**, *21*, 4949.
- [14] J. Chen, C. K. Tee, M. Shtein, J. Anthony, D. C. Martin, *J. Appl. Phys.* **2008**, *103*, 114513.
- [15] Y. Sun, L. Zhang, Z. Ahmed, M. Chan, *Org. Electron.* **2015**, *27*, 192.
- [16] A. Di Carlo, F. Piacenza, A. Bolognesi, B. Stadlober, H. Maresch, *Appl. Phys. Lett.* **2005**, *86*, 263501.
- [17] A. B. Chwang, C. D. Frisbie, *J. Appl. Phys.* **2001**, *90*, 1342.
- [18] T. Meier, H. Bässler, A. Köhler, *Adv. Opt. Mater.* **2021**, *9*, 2100115.
- [19] T. W. Kelley, C. D. Frisbie, *J. Phys. Chem. B* **2001**, *105*, 4538.
- [20] A. Bolognesi, M. Berliocchi, M. Manenti, A. DiCarlo, P. Lugli, K. Lmimouni, C. Dufour, *IEEE Trans. Electron Devices* **2004**, *51*, 1997.
- [21] G. Horowitz, *Adv. Funct. Mater.* **2003**, *13*, 53.
- [22] H. Kobayashi, Y. Tokita, *Appl. Phys. Express* **2015**, *8*, 051602.
- [23] S. S. Lee, J. M. Mativetsky, M. A. Loth, J. E. Anthony, Y.-L. Loo, *ACS Nano* **2012**, *6*, 9879.
- [24] S. Wo, R. L. Headrick, J. E. Anthony, *J. Appl. Phys.* **2012**, *111*, 073716.
- [25] R. R. Lunt, J. B. Benziger, S. R. Forrest, *Adv. Mater.* **2010**, *22*, 1233.
- [26] K. Shi, A. T. Healy, I. J. Curtin, T. Zhang, D. A. Blank, R. J. Holmes, *J. Phys. Chem. C* **2022**, *126*, 4792.
- [27] S. Caria, E. Da Como, M. Murgia, R. Zamboni, P. Melpignano, V. Biondo, *J. Phys.: Condens. Matter* **2006**, *18*, S2139.
- [28] X. Zhang, H. Dong, W. Hu, *Adv. Mater.* **2018**, *30*, 1801048.
- [29] M. Nonnenmacher, M. P. O'Boyle, H. K. Wickramasinghe, *Appl. Phys. Lett.* **1991**, *58*, 2921.
- [30] V. Palermo, M. Palma, P. Samorì, *Adv. Mater.* **2006**, *18*, 145.
- [31] A. Axt, I. M. Hermes, V. W. Bergmann, N. Tausendpfund, S. A. L. Weber, *Beilstein J. Nanotechnol.* **2018**, *9*, 1809.
- [32] K. Puntambekar, J. Dong, G. Haugstad, C. D. Frisbie, *Adv. Funct. Mater.* **2006**, *16*, 879.
- [33] H. Huang, H. Wang, J. Zhang, D. Yan, *Appl. Phys. A* **2009**, *95*, 125.
- [34] S. Yogeve, R. Matsubara, M. Nakamura, Y. Rosenwaks, *Org. Electron.* **2010**, *11*, 1729.
- [35] M. Tello, M. Chiesa, C. M. Duffy, H. Siringhaus, *Adv. Funct. Mater.* **2008**, *18*, 3907.
- [36] I. Vladimirov, M. Kellermeier, T. Geßner, Z. Molla, S. Grigorian, U. Pietsch, L. S. Schaffroth, M. Kühn, F. May, R. T. Weitz, *Nano Lett.* **2018**, *18*, 9.
- [37] S. K. Park, J. H. Kim, S. Y. Park, *Adv. Mater.* **2018**, *30*, 1704759.
- [38] H. Yan, Y. Li, J.-K. Qin, B. Xu, P.-A. Hu, L. Zhen, C.-Y. Xu, *Small* **2021**, *17*, 2007739.
- [39] P. Hu, X. He, H. Jiang, *InfoMat* **2021**, *3*, 613.
- [40] X. Zhang, X. Zhao, L. Rao, J. Zhang, M. Xiao, D. Zhu, C. Li, X. Shi, J. Liu, L. Jiang, *Nano Res.* **2022**, *15*, 858.
- [41] S. Schiefer, B. Zimmermann, U. Würfel, *J. Appl. Phys.* **2014**, *115*, 044506.
- [42] K. Nakano, Y. Chen, K. Tajima, *AIP Adv.* **2019**, *9*, 125205.
- [43] T. He, Y. Wu, G. D'Avino, E. Schmidt, M. Stolte, J. Cornil, D. Beljonne, P. P. Ruden, F. Würthner, C. D. Frisbie, *Nat. Commun.* **2018**, *9*, 2141.
- [44] Y. M. Lee, J. W. Kim, H. Min, T. G. Lee, Y. Park, *Curr. Appl. Phys.* **2011**, *11*, 1168.
- [45] S. Verlaak, P. Heremans, *Phys. Rev. B* **2007**, *75*, 115127.
- [46] I. Vladimirov, M. Kühn, T. Geßner, F. May, R. T. Weitz, *Sci. Rep.* **2018**, *8*, 14868.
- [47] L. H. Jimison, M. F. Toney, I. McCulloch, M. Heeney, A. Salleo, *Adv. Mater.* **2009**, *21*, 1568.
- [48] J. W. Orton, M. J. Powell, *Rep. Prog. Phys.* **1980**, *43*, 1263.
- [49] R. T. Weitz, K. Amsharov, U. Zschieschang, E. B. Villas, D. K. Goswami, M. Burghard, H. Dosch, M. Jansen, K. Kern, H. Klauk, *J. Am. Chem. Soc.* **2008**, *130*, 4637.
- [50] A. K. Hailey, S.-Y. Wang, Y. Chen, M. M. Payne, J. E. Anthony, V. Podzorov, Y.-L. Loo, *Adv. Funct. Mater.* **2015**, *25*, 5662.
- [51] L. G. Kaake, P. F. Barbara, X.-Y. Zhu, *J. Phys. Chem. Lett.* **2010**, *1*, 628.
- [52] X. Li, A. Kadeshchuk, I. I. Fishchuk, W. T. T. Smaal, G. Gelinck, D. J. Broer, J. Genoe, P. Heremans, H. Bässler, *Phys. Rev. Lett.* **2012**, *108*, 66601.
- [53] I. Vladimirov, Dissertation, Technische Universität Braunschweig, Braunschweig, Germany **2016**.
- [54] N. B. Kotadiya, A. Mondal, P. W. M. Blom, D. Andrienko, G.-J. A. H. Wetzelaer, *Nat. Mater.* **2019**, *18*, 1182.
- [55] M. Kettner, M. Zhou, J. Brill, P. W. M. Blom, R. T. Weitz, *ACS Appl. Mater. Interfaces* **2018**, *10*, 35449.
- [56] U. Zschieschang, K. Amsharov, M. Jansen, K. Kern, H. Klauk, R. T. Weitz, *Org. Electron.* **2015**, *26*, 340.
- [57] Y. Gao, W. Xu, S.-W. Zhang, T. Fan, M. Zhang, A. Ran, X. Zhang, F. Kang, G. Wei, *Small* **2022**, *18*, 2106083.
- [58] K. Liang, D. Li, H. Ren, M. Zhao, H. Wang, M. Ding, G. Xu, X. Zhao, S. Long, S. Zhu, P. Sheng, W. Li, X. Lin, B. Zhu, *Nano-Micro Lett.* **2021**, *13*, 164. Published Online: Aug. 3, 2021.
- [59] S. Zhang, J. Pang, Q. Cheng, F. Yang, Y. Chen, Y. Liu, Y. Li, T. Gemming, X. Liu, B. Ibarlucea, J. Yang, H. Liu, W. Zhou, G. Cuniberti, M. H. Rummeli, *InfoMat* **2021**, *3*, 1455.



- [60] Y. Wang, J. Pang, Q. Cheng, L. Han, Y. Li, X. Meng, B. Ibarlucea, H. Zhao, F. Yang, H. Liu, H. Liu, W. Zhou, X. Wang, M. H. Rummeli, Y. Zhang, G. Cuniberti, *Nano-Micro Lett.* **2021**, *13*, 143.
- [61] L. S. Schaffroth, J. Lenz, V. Giegold, M. Kögl, A. Hartschuh, R. T. Weitz, *Adv. Mater.* **2019**, *31*, 1808309.
- [62] L. Renn, L. S. Walter, K. Watanabe, T. Taniguchi, R. T. Weitz, *Adv. Mater. Inter.* **2022**, *9*, 2101701.
- [63] C. D. Dimitrakopoulos, P. Malenfant, *Adv. Mater.* **2002**, *14*, 99.
- [64] D. Nečas, P. Klapetek, *Cent. Eur. J. Phys.* **2012**, *10*, 181.